ACS Photonics
Letter
Cite This: ACS Photonics 2018, 5, 4764−4768
pubs.acs.org/journal/apchd5

Order and Disorder Embedded in a Spectrally Interleaved Metasurface

Michael Yannai,[†] Elhanan Maguid,[†] Arkady Faerman,[†] Qitong Li,[‡] Jung-Hwan Song,[‡] Vladimir Kleiner,[†] Mark L. Brongersma,[‡] and Erez Hasman*,[†]

[†]Micro and Nanooptics Laboratory, Faculty of Mechanical Engineering, and Russell Berrie Nanotechnology Institute, Technion−Israel Institute of Technology, Haifa 3200003, Israel

[‡]Geballe Laboratory for Advanced Materials, Stanford University, 476 Lomita Mall, Stanford, California 94305, United States

ABSTRACT: Metasurfaces enable the manipulation of light's disorder strength in a two-dimensional photonic system. Here we report on the spectral interleaving of an ordered and a disordered system within a geometric phase metasurface. The efficiency of prevalent interleaving techniques is limited by the number of functions incorporated within the metasurface. We present a shared-aperture extinction cross-section approach relying on interleaving of spectrally selective nanoantenna arrays, each having a large extinction cross-section, thus allowing to overcome this limitation. Using this approach, we realize a silicon-based spectral interleaving metasurface for spectrum-dependent disguise, holographic tagging, and imaging of a target object. The shared-aperture extinction cross-section concept opens the path for the generation of multiple, efficient, and spectrally resolved functions in a two-dimensional photonic system. The presented order−disorder interleaving approach offers new prospects for the manipulation of light's entropy.

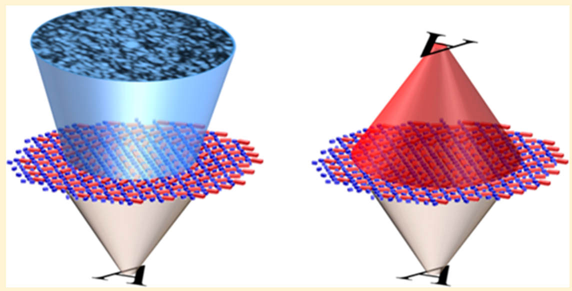

KEYWORDS: *metasurfaces, disorder, random media, multifunctional, multispectral*

The incorporation of multiple functions in a single nanophotonic device poses a unique physical and conceptual challenge. The ability to combine multiple functions operating at the same frequency region in a single broadband metasurface was demonstrated, enabling the implementation of remote sensing, communication, and spectropolarimetry nanodevices.[1−6] Multitasking was achieved by use of various multiplexing techniques, such as segmentation and interleaving of sparse antenna-arrays implemented within a shared-aperture metasurface. Metasurfaces consist of arrays of subwavelength nanoantennas, capable of manipulating light by controlling the local properties of an incident electromagnetic wave.[7−16] Controlling the spectral resonance of nanoantennas was shown,[17−19] enabling the spatial multiplexing of spectrally sensitive nanoantennas and paving the route for the generation of multispectral metasurfaces.[20−27]

Recently, a demonstration of the photonic transition from photonic spin Hall effect to a random Rashba effect was realized via disordered geometric phase metasurfaces.[28] This transition is attained by varying the amount of allowable random rotation of the antennas constituting the metasurface: from ordered to completely random rotation. As the order parameter approaches unity, corresponding to a completely random metasurface, a random Rashba effect is observed, which is manifested by numerous modes filling the entire momentum-space. Moreover, random metasurfaces were utilized to control the propagation of light.[29−31] The control over the disorder strength in nanostructures enables the manipulation of the entropy of light in a two-dimensional photonic system.

Here we report on the incorporation of an ordered and a disordered system in an all-dielectric metasurface by using a spectral interleaving technique. The proposed spectrally interleaved nanodevice is utilized to camouflage a target object at a certain wavelength, while imaging it at a different wavelength (Figure 1a). Here, the disordered system is described by a random phase distribution, while an analytic phase profile (e.g., lens, prism) constitutes an ordered system. The conventional interleaving approaches toward multifunctionality have an efficiency η that is fundamentally limited by the number of functions N incorporated within the metasurface. The efficiency of broadband and spectrally interleaved nanoantenna arrays is bounded by $\eta \approx 1/N^2$ and $\eta \approx 1/N$, respectively.[1,3,29] Generally, the extinction cross-section of a nanoantenna can be much larger than its physical cross-section, which is defined by a characteristic dimension.[17−19] We present a shared-aperture extinction cross-section approach, interleaving of spectrally selective nanoantenna arrays, each having a large extinction cross-section, thus allowing to overcome this efficiency limitation (Figure 2a).

Spectrally interleaved geometric phase metasurfaces (SIGPMs) based on the shared-aperture extinction cross-section approach are implemented using Si-based subwavelength scale nanoantennas

Received: August 15, 2018
Published: November 12, 2018

DOI: 10.1021/acsphotonics.8b01138
ACS Photonics 2018, 5, 4764−4768

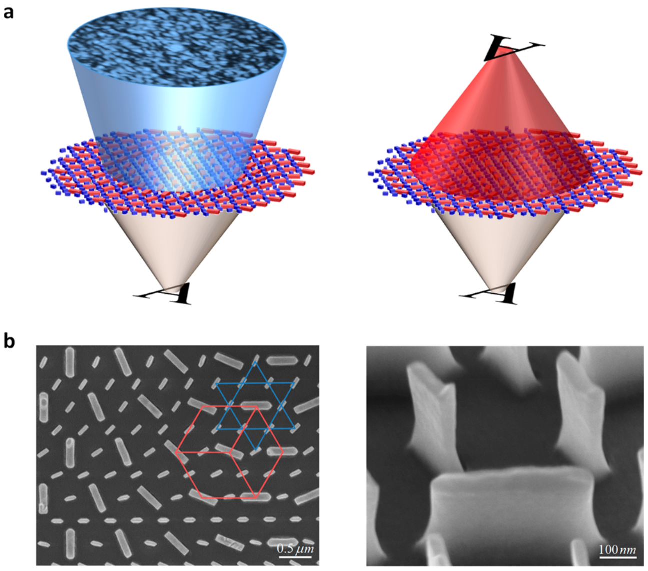

Figure 1. Order and disorder interleaving concept. (a) Spectrally interleaved geometric phase metasurface (SIGPM) encompassing two wavelength-dependent functions: a diffuser at one wavelength (left, blue) and a lens at the second (right, red). (b) SEM images of the fabricated dual-function SIGPM. The first nanoantenna with in-plane dimensions of 190 × 50 nm has peak efficiency at a wavelength of 600 nm and is arranged into a Kagome lattice with a lattice constant of 400 nm. The second antenna has in-plane dimensions of 440 × 120 nm and peak efficiency at a wavelength of 820 nm and is arranged into a hexagonal lattice with a lattice constant of 800 nm. Blue and red lines highlight the Kagome and hexagonal lattice structures, respectively.

(Figure 1b), offering low loss and arbitrary control over the phase profile.

The SIGPMs are composed of spectrally selective anisotropic nanoantennas which generate a local wavelength-dependent phase delay $\phi_g(x, y) = -2\sigma\theta(x, y)$. Here, $\theta(x, y)$ is the in-plane orientation angle of the nanoantennas,[7,8,32,33] and $\sigma = \pm 1$ denotes the sign of the spin angular momentum of light ($\hbar\sigma$), i.e., right ($\sigma = 1$) or left ($\sigma = -1$) circular polarization.[34,35]

SIGPMs are generated by the incorporation of two or more nanoantenna types, having adequately spectrally separated quasi-orthogonal modes, into optimally spaced interleaved arrays. Here, the structure is formed from a 400 nm thick crystalline Si layer consisting of two interleaved arrays, each with its own resonant nanoantenna geometry (Figure 1b). The antennas' geometry is determined using finite-difference time-domain (FDTD) simulations of a single-function linear phase antenna array and is optimized to achieve the desired narrowband diffraction efficiency spectrum. Then, the power flow through each antenna and its extinction cross-section are analyzed at the antenna's peak efficiency wavelength, facilitating the selection of the geometry having the largest scattering efficiency and determining the optimal antenna spacing. Finally, for interleaving the two antenna arrays, a Kagome and hexagonal lattice are used as they offer a relatively high packing factor and allow for maximal use of each antenna's extinction cross-section. Note that no antennas need to be moved or removed in this interleaving process. Figure 2b depicts FDTD simulations showing the field distribution and power flow for the proposed SIGPM, at both peak efficiency wavelengths. Each spectral nanoantenna possesses an enhanced extinction cross-section which can span the neighboring lattice sites of the interleaved lattice (Figure 2b, top images). This cross-sectional behavior holds also for the spectrally interleaved nanoantennas (Figure 2b, bottom images). Furthermore, it is evident that interleaving the two nanoantenna arrays has little or no effect on the modes' shape, as compared to the single-antenna metasurface, with negligible cross-talk between the two types of antennas. Consequently, a highly efficient SIGPM can be designed by utilizing the shared-aperture extinction cross-section approach. A dual-function SIGPM with orthogonal linear phase profiles was experimentally characterized, and separated diffraction orders were observed. The metasurface was illuminated with circularly polarized light at both peak efficiency wavelengths, and the spin-flipped momentum-space image was measured using a circular analyzer. A negligible cross-talk between the two arrays of spectral nanoantennas was clearly observed, as indicated by the ratio of the diffraction orders' intensities (Figure 2c).

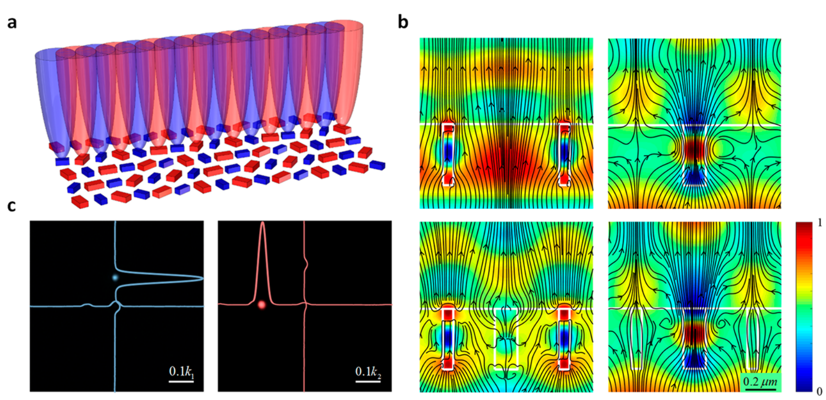

Figure 2. Extinction cross-section and cross-talk of SIGPM. (a) Illustration of the funnel-like cross-sectional behavior of the single antenna, allowing the incorporation of a second function to the metasurface. (b) FDTD simulations of single- and dual-function SIGPMs depicting a two-dimensional cross-section over one unit cell. Shown here are the real part of the electric field in the direction normal to the section's plane ($Re\{E_n\}$, color) and the in-plane electromagnetic power flow, represented by the real part of the transverse Poynting vector ($Re\{\mathbf{P}_t\}$, black lines). Top and bottom images correspond to single- and dual-function SIGPMs, respectively, illuminated at the short (left) and long wavelengths (right). The nanoantenna's location and Si−glass interface are marked in white; input field is injected from the bottom. The ratio of the extinction cross-section to the physical cross-section (antenna's area) was calculated from the FDTD simulations and was found to be 14.4 for the short-wavelength antennas and 3.5 for the long-wavelength antennas. (c) Momentum-space measurements of a linear phase dual-function SIGPM, illuminated at a wavelength of λ_1 = 600 nm (left) and λ_2 = 820 nm (right). Images are false-colored. Scale bars correspond to the illumination wavelength ($k_i = 2\pi/\lambda_i$).

DOI: 10.1021/acsphotonics.8b01138
ACS Photonics 2018, 5, 4764−4768

To evaluate the performance of the SIGPM, we calculated the fractional diffraction efficiency (FDE) spectra $\mathrm{FDE}_i = I_i/\sum_j I_j$, for both single-function and dual-function SIGPMs using FDTD simulations (Figure 3a). Here, I_i is the intensity of the desired ith diffraction order, and the summation is carried over all the emerging diffraction orders, including the non-interacting zero order. A simulated average spectral transmittance of 80% is obtained for the single- and dual-function SIGPMs, resulting in peak diffraction order efficiencies of 60% and 70% for the short- and long-wavelength channels of the dual-function SIGPM, respectively. Here, the diffraction order efficiency at a certain wavelength is obtained by multiplying the FDE by the SIGPM's transmittance at that wavelength. Figure 3b depicts the measured FDE spectra for the fabricated SIGPM. Incorporating the two functions into a single device has very little effect on the modes' spectral shape and peak efficiency. In comparison to the simulated spectra (Figure 3a), the loss of efficiency and spectral shifts are attributed to fabrication scaling errors in the nanoantennas' dimensions. FDE spectra obtained from FDTD simulations for the fabricated SIGPM including the scaling errors were found to be in good agreement with the experiments (Figure 3c). We investigated the normalized per-function peak FDE, obtained using the shared-aperture extinction cross-section approach, and compared it with different techniques for generating a multifunctional metasurface (Figure 3d).

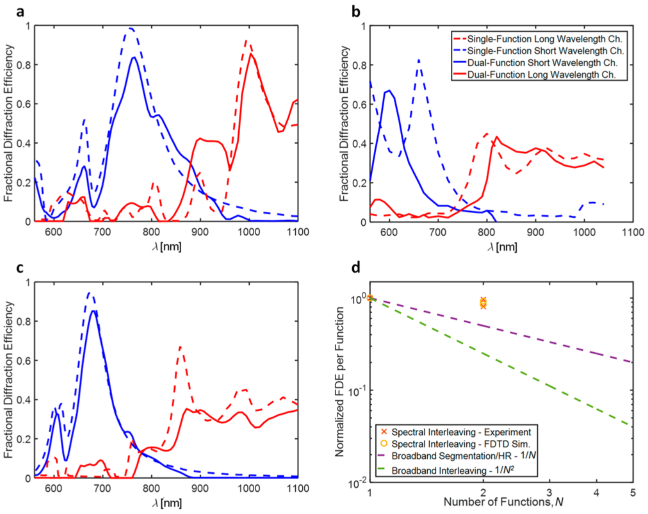

Figure 3. FDE spectra characterization. FDTD simulations (a) and measurements (b) showing FDE spectra for single-function (dashed lines) and dual-function (lines) SIGPMs. The designed antennas' in-plane dimensions are 210 × 70 nm and 470 × 150 nm, with periods of 385 and 770 nm, respectively, and antenna height of 400 nm. Missing data points in Figure 3b are due to a lack of adequate source at these wavelengths (1040−1100 nm). (c) FDE spectra obtained from FDTD simulations of the fabricated SIGPMs including the scaling errors. The dimensions were obtained from SEM images of the fabricated SIGPM (see Figure 1b caption). (d) Comparison of different techniques for generating a multifunctional metasurface, illustrating the per-function FDE dependence on the number of functions, N. Circles represent FDTD simulations for single-function and dual-function SIGPMs, where the FDE values were taken at the peak efficiency wavelength and normalized to the appropriate single-function FDE. Crosses represent measured FDE corresponding to the data in (b), also normalized in a similar fashion. Data are presented in log−log scale. Note, each spectral function is represented by a separate data point, in both simulation and experiment.

The normalized FDE with respect to a single-function metasurface pronounces the effect of the multiplexing processes. For the segmentation approach, as well as the harmonic response (HR) technique, which is based on the use of Dammann gratings, a $1/N$ decrease in efficiency is expected. Furthermore, the efficiency of the broadband interleaving technique decreases according to $1/N^2$.[1,3,29] The shared-aperture extinction cross-section approach allows overcoming the $1/N$ limit, i.e., a multi-functional multispectral metasurface limited only by the individual resonators' efficiency.

We incorporated ordered and disordered phase profiles using a dual-function SIGPM, with a random phase distribution at the short-wavelength function and a lens phase profile at the long-wavelength function. When this metasurface was illuminated at a wavelength of 600 nm, a diffuse intensity pattern was observed (Figure 4a, top image). Switching to a wavelength of 820 nm, a diffraction-limited peak was observed 250 μm behind the metasurface, corresponding to the assigned focal length of the meta-lens (Figure 4a, bottom image). To further demonstrate this SIGPM's capabilities, a target object was introduced before the sample. When illuminated at a wavelength of 600 nm, no image was observed (Figure 4b, top); however, when illuminated at a wavelength of 820 nm, the image of the target object was revealed (Figure 4b, bottom). The information passing through the SIGPM at the short wavelength is dispersed into the entire momentum-space by the disordered phase function; therefore, it cannot be reconstructed by a neutral observer, in contrast to a conventional meta-lens. We also realized a SIGPM in which the long-wavelength phase profile was replaced by a hologram of the Greek letter sigma, designed using the Gerchberg−Saxton algorithm.[36] Upon illumination of the metasurface at a wavelength of 820 nm, the desired hologram was attained (Figure 4c, bottom), and a diffuse intensity pattern was observed at a wavelength of 600 nm (Figure 4c, top).

The shared-aperture extinction cross-section concept opens the path for the generation of multiple, efficient, and spectrally resolved functions in a two-dimensional photonic system. The presented order−disorder interleaving approach offers new prospects for spectrum-dependent disguise, imaging, and tagging, with applications in counterfeit prevention and the security industry.

■ METHODS

Sample Fabrication. We prepare a 400-nm-thick single-crystalline silicon slab on a borosilicate glass substrate in a two-step dry etching process. A 20-μm-thick single-crystalline silicon on borosilicate glass wafer (Plan Optik AG) is first coarsely etched down to ∼2 μm by deep reactive ion etching. The thickness of the wafer is then progressively thinned to 400 nm in several rounds of precise reactive ion etching. A 70-nm-thick hydrogen silsesquioxane (HSQ) layer serves as a negative tone electron beam resist layer and is spin coated on the silicon slab. A conductive polymer layer (E-Spacer 300Z) is also deposited in order to reduce electron charging effects during the electron beam lithography process (JEOL 6300 100 kV system). The typical electron beam dose is set to ∼2000 $\mu C\ cm^{-2}$, and the development is performed in 25% tetramethylammonium hydroxide (TMAH) for 2 min. Precise reactive ion etching is conducted again to transfer the HSQ hard mask patterns into the silicon slab, and the remaining HSQ hard mask pattern is ultimately removed using a diluted 2% hydrogen fluoride (HF) solution for 1 min.

DOI: 10.1021/acsphotonics.8b01138
ACS Photonics 2018, 5, 4764−4768

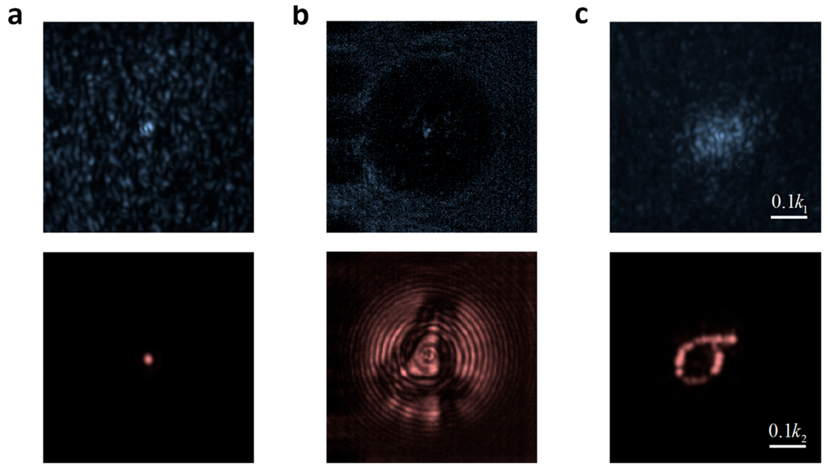

Figure 4. Wavelength-dependent disguise, imaging, and tagging using SIGPM. (a) Point spread function characterization of a dual-function SIGPM with a random phase distribution in the short-wavelength function (top image) and a lens phase profile in the long-wavelength function (bottom image). Both images were taken at the lens focal plane, 250 μm behind the SIGPM. (b) Imaging via the SIGPM containing the lens and random phase. The object is a figure four taken from a USAF 1951 bar target. When illuminated at the short wavelength (top), no image was visible; only at the long wavelength (bottom) did the image appear. For this measurement, the setup was such that the object is imaged to the metasurface, and subsequently both are imaged to the camera. (c) Measurement of a dual-function SIGPM with a random phase distribution in the short-wavelength function (top image) and a hologram of the Greek letter sigma (σ) at the long-wavelength. Images were taken at the momentum-space. Top images were taken at a wavelength of 600 nm; bottom images at 820 nm. Images are false-colored.

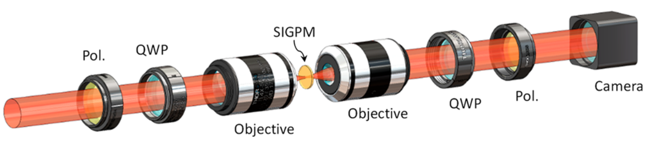

Figure 5. Experimental setup for characterizing the SIGPMs. Pol., polarizer; QWP, quarter-wave plate.

Measurement Procedure. Figure 5 depicts the basic setup used in our experiments. The input beam, generated by a supercontinuum laser source (Fianium Supercontinuum SC450), was temporally modulated by an acousto-optic modulator (Fianium AOTF V1) facilitating the use of multiwavelength laser light. The beam was then spatially filtered and collimated. A linear polarizer (Pol.) followed by a quarter-wave plate (QWP) served as a circular polarizer. Two objectives in a 4f configuration are used to focus light onto the sample (SIGPM) and collect the scattered light, respectively. For the experiments depicted in Figures 2c and 4, a polarizer−analyzer in a cross-polarized configuration is introduced, to eliminate the noninteracting diffraction order. Finally, the images are captured using a CMOS camera. Measurements of the FDE and transmittance spectra are carried out by removing the polarizer−analyzer.

AUTHOR INFORMATION

Corresponding Author

*E-mail: mehasman@technion.ac.il.

ORCID

Elhanan Maguid: 0000-0001-6972-1816

Erez Hasman: 0000-0002-3419-8815

Notes

The authors declare no competing financial interest.

ACKNOWLEDGMENTS

The authors gratefully acknowledge financial support from the United States−Israel Binational Science Foundation (BSF), the Israel Science Foundation (ISF), and the U.S. Air Force Office of Scientific Research (FA9550-18-1-0208) through their program on Photonic Metamaterials. Part of the fabrication was performed at the Micro-Nano Fabrication & Printing Unit (MNF&PU), Technion. Part of this work was performed at the Stanford Nano Shared Facilities (SNSF), supported by the National Science Foundation under award ECCS-1542152. J.-H.S. is supported by the Basic Science Research Program through the National Research Foundation of Korea (NRF) funded by the Ministry of Education (NRF-2016R1A6A3A03012480).

REFERENCES

(1) Maguid, E.; Yulevich, I.; Veksler, D.; Kleiner, V.; Brongersma, M. L.; Hasman, E. Photonic Spin-Controlled Multifunctional Shared-Aperture Antenna Array. *Science* **2016**, *352*, 1202−1206.

(2) Mehmood, M. Q.; Mei, S.; Hussain, S.; Huang, K.; Siew, S. Y.; Zhang, L.; Zhang, T.; Ling, X.; Liu, H.; Teng, J.; Danner, A.; Zhang, S.; Qiu, C. W. Visible-Frequency Metasurface for Structuring and Spatially Multiplexing Optical Vortices. *Adv. Mater.* **2016**, *28*, 2533−2539.

(3) Maguid, E.; Yulevich, I.; Yannai, M.; Kleiner, V.; L Brongersma, M. L.; Hasman, E. Multifunctional Interleaved Geometric-Phase Dielectric Metasurfaces. *Light: Sci. Appl.* **2017**, *6*, No. e17027.

(4) Ding, F.; Pors, A.; Chen, Y.; Zenin, V. A.; Bozhevolnyi, S. I. Beam-Size-Invariant Spectropolarimeters Using Gap-Plasmon Metasurfaces. *ACS Photonics* **2017**, *4*, 943−949.

(5) Khorasaninejad, M.; Capasso, F. Metalenses: Versatile Multifunctional Photonic Components. *Science* **2017**, *358*, No. eaam8100.

(6) Chen, Y.; Ding, F.; Coello, V.; Bozhevolnyi, S. I. On-Chip Spectropolarimetry by Fingerprinting with Random Surface Arrays of Nanoparticles. *ACS Photonics* **2018**, *5*, 1703−1710.

DOI: 10.1021/acsphotonics.8b01138
ACS Photonics 2018, 5, 4764−4768

(7) Bomzon, Z.; Kleiner, V.; Hasman, E. Pancharatnam−Berry Phase in Space-Variant Polarization-State Manipulations with Subwavelength Gratings. *Opt. Lett.* **2001**, *26*, 1424−1426.
(8) Bomzon, Z.; Biener, G.; Kleiner, V.; Hasman, E. Space-Variant Pancharatnam−Berry Phase Optical Elements with Computer-Generated Subwavelength Gratings. *Opt. Lett.* **2002**, *27*, 1141−1143.
(9) Papakostas, A.; Potts, A.; Bagnall, D. M.; Prosvirnin, S. L.; Coles, H. J.; Zheludev, N. I. Optical Manifestations of Planar Chirality. *Phys. Rev. Lett.* **2003**, *90*, 107404.
(10) Kildishev, A. V.; Boltasseva, A.; Shalaev, V. M. Planar Photonics with Metasurfaces. *Science* **2013**, *339*, 1232009.
(11) Liu, L.; Zhang, X.; Kenney, M.; Su, X.; Xu, N.; Ouyang, C.; Shi, Y.; Han, J.; Zhang, W.; Zhang, S. Broadband Metasurfaces with Simultaneous Control of Phase and Amplitude. *Adv. Mater.* **2014**, *26*, 5031−5036.
(12) Lin, D.; Fan, P.; Hasman, E.; Brongersma, M. L. Dielectric Gradient Metasurface Optical Elements. *Science* **2014**, *345*, 298−302.
(13) Shalaev, M. I.; Sun, J.; Tsukernik, A.; Pandey, A.; Nikolskiy, K.; Litchinitser, N. M. High-Efficiency All-Dielectric Metasurfaces for Ultracompact Beam Manipulation in Transmission Mode. *Nano Lett.* **2015**, *15*, 6261−6266.
(14) Minovich, A. E.; Miroshnichenko, A. E.; Bykov, A. Y.; Murzina, T. V.; Neshev, D. N.; Kivshar, Y. S. Functional and Nonlinear Optical Metasurfaces. *Laser Photonics Rev.* **2015**, *9*, 195−213.
(15) Wang, Q.; Rogers, E. T. F.; Gholipour, B.; Wang, C.; Yuan, G.; Teng, J.; Zheludev, N. I. Optically Reconfigurable Metasurfaces And Photonic Devices Based on Phase Change Materials. *Nat. Photonics* **2016**, *10*, 60−65.
(16) Yue, F.; Wen, D.; Zhang, C.; Gerardot, B. D.; Wang, W.; Zhang, S.; Chen, X. Multichannel Polarization-Controllable Superpositions of Orbital Angular Momentum States. *Adv. Mater.* **2017**, *29*, 1603838.
(17) Staude, I.; Miroshnichenko, A. E.; Decker, M.; Fofang, N. T.; Liu, S.; Gonzales, E.; Dominguez, J.; Luk, T. S.; Neshev, D. N.; Brener, I.; Kivshar, Y. Tailoring Directional Scattering through Magnetic and Electric Resonances in Subwavelength Silicon Nanodisks. *ACS Nano* **2013**, *7*, 7824−7832.
(18) Ee, H. S.; Kang, J. H.; Brongersma, M. L.; Seo, M. K. Shape-Dependent Light Scattering Properties of Subwavelength Silicon Nanoblocks. *Nano Lett.* **2015**, *15*, 1759−1765.
(19) Kuznetsov, A. I.; Miroshnichenko, A. E.; Brongersma, M. L.; Kivshar, Y. S.; Luk'yanchuk, B. Optically Resonant Dielectric Nanostructures. *Science* **2016**, *354*, aag2472.
(20) Arbabi, A.; Horie, Y.; Ball, A. J.; Bagheri, M.; Faraon, A. Subwavelength-Thick Lenses with High Numerical Apertures and Large Efficiency Based on High-Contrast Transmitarrays. *Nat. Commun.* **2015**, *6*, 7069.
(21) Wang, B.; Dong, F.; Li, Q. T.; Yang, D.; Sun, C.; Chen, J.; Song, Z.; Xu, L.; Chu, W.; Xiao, Y. F.; Gong, Q.; Li, Y. Visible-Frequency Dielectric Metasurfaces for Multiwavelength Achromatic and Highly Dispersive Holograms. *Nano Lett.* **2016**, *16*, 5235−5240.
(22) Huang, C.; Pan, W.; Ma, X.; Luo, X. Multi-Spectral Metasurface for Different Functional Control of Reflection Waves. *Sci. Rep.* **2016**, *6*, 23291.
(23) Arbabi, E.; Arbabi, A.; Kamali, S. M.; Horie, Y.; Faraon, A. Multiwavelength Polarization-Insensitive Lenses Based on Dielectric Metasurfaces With Meta-Molecules. *Optica* **2016**, *3*, 628−633.
(24) Avayu, O.; Almeida, E.; Prior, Y.; Ellenbogen, T. Composite Functional Metasurfaces for Multispectral Achromatic Optics. *Nat. Commun.* **2017**, *8*, 14992.
(25) Wang, B.; Dong, F.; Yang, D.; Song, Z.; Xu, L.; Chu, W.; Gong, Q.; Li, Y. Polarization-Controlled Color-Tunable Holograms with Dielectric Metasurfaces. *Optica* **2017**, *4*, 1368−1371.
(26) Shi, Z.; Khorasaninejad, M.; Huang, Y. W.; Roques-Carmes, C.; Zhu, A. Y.; Chen, W. T.; Sanjeev, V.; Ding, Z. W.; Tamagnone, M.; Chaudhary, K.; Devlin, R. C.; Qiu, C. W.; Capasso, F. Single-Layer Metasurface with Controllable Multiwavelength Functions. *Nano Lett.* **2018**, *18*, 2420−2427.
(27) Arbabi, E.; Arbabi, A.; Kamali, S. M.; Horie, Y.; Faraon, A. Multiwavelength Metasurfaces through Spatial Multiplexing. *Sci. Rep.* **2016**, *6*, 32803.
(28) Maguid, E.; Yannai, M.; Faerman, A.; Yulevich, I.; Kleiner, V.; Hasman, E. Disorder-Induced Optical Transition from Spin Hall to Random Rashba Effect. *Science* **2017**, *358*, 1411−1415.
(29) Veksler, D.; Maguid, E.; Shitrit, N.; Ozeri, D.; Kleiner, V.; Hasman, E. Multiple Wavefront Shaping by Metasurface Based on Mixed Random Antenna Groups. *ACS Photonics* **2015**, *2*, 661−667.
(30) Pors, A.; Ding, F.; Chen, Y.; Radko, I. P.; Bozhevolnyi, S. I. Random-Phase Metasurfaces at Optical Wavelengths. *Sci. Rep.* **2016**, *6*, 28448.
(31) Jang, M.; Horie, Y.; Shibukawa, A.; Brake, J.; Liu, Y.; Kamali, S. M.; Arbabi, A.; Ruan, H.; Faraon, A.; Yang, C. Wavefront Shaping with Disorder-Engineered Metasurfaces. *Nat. Photonics* **2018**, *12*, 84−90.
(32) Pancharatnam, S. Generalized Theory of Interference and Its Applications. *Proc. - Indian Acad. Sci., Sect. A* **1956**, *A44*, 398−417.
(33) Berry, M. V. Quantal Phase Factors Accompanying Adiabatic Changes. *Proc. R. Soc. London, Ser. A* **1984**, *392*, 45−57.
(34) Bliokh, K. Y.; Rodríguez-Fortuño, F. J.; Nori, F.; Zayats, A. V. Spin−orbit Interactions of Light. *Nat. Photonics* **2015**, *9*, 796−808.
(35) Bliokh, K. Y.; Smirnova, D.; Nori, F. Quantum Spin Hall Effect of Light. *Science* **2015**, *348*, 1448−1451.
(36) Gerchberg, R. W.; Saxton, W. O. A Practical Algorithm for the Determination of Phase from Image and Diffraction Plane Pictures. *Optik (Stuttg).* **1972**, *35*, 237−246.

DOI: 10.1021/acsphotonics.8b01138
ACS Photonics 2018, 5, 4764−4768